

Article

The Seasonal Variation of the Anomalously High Salinity at Subsurface Salinity Maximum in Northern South China Sea from Argo Data

Hui Shen ¹ , Li Li ^{1,2} , Jianlong Li ³, Zhiguo He ^{1,4} and Yuezhong Xia ^{1,2,*} 

¹ Institute of Port and Offshore Engineering, Ocean College, Zhejiang University, Zhoushan 316021, China; ocsenhui@zju.edu.cn (H.S.); lilizju@zju.edu.cn (L.L.); hezhiguo@zju.edu.cn (Z.H.)

² State Key Laboratory of Satellite Ocean Environment Dynamics, Second Institute of Oceanography, SOA, Hangzhou 310058, China

³ College of Information Science & Electronic Engineering, Zhejiang University, Hangzhou 310027, China; jlli@zju.edu.cn

⁴ Engineering Research Center of Oceanic Sensing Technology and Equipment, Zhejiang University, Zhoushan 316021, China

* Correspondence: yzxia@zju.edu.cn; Tel.: +86-13588373750

Abstract: The large variations in salinity at the salinity maximum in the northern South China Sea (NSCS), as an indicator for the changes in the Kuroshio intrusion (KI), play an important role in the hydrological cycle. The high salinity here is more than 34.65 at the salinity maximum and is intriguing. In the past, the salinity was difficult to trace in the entire NSCS over long periods due to a lack of high-quality observations. However, due to the availability of accumulated temperature and salinity (T-S) profiles from the Argo program, it is now possible to capture subsurface-maximum data on a large spatiotemporal scale. In this study, the salinity maximum distributed in the subsurface of 80 to 200 m at a density of 23.0–25.5 σ_θ was extracted from decades of Argo data (on the different pressure surfaces, 2006–2019). We then further studied the spatial distribution and seasonal variation of the salinity maximum and its anomalously high salinity. The results suggest that a high salinity (salinity > 34.65, most of which is located at the shallow depths < 100 m) at the subsurface salinity-maximum layer often occurs in the NSCS, especially near the Luzon Strait, which accounts for about 23% of the total salinity maximum. In winter, the anomalously high salinity at the shallow subsurface salinity maximum can extend to the south of 17° N, while it rarely reaches 18° N and tends to locate at deeper waters in summer. The T-S values of the anomalously high-salinity water are between the mean T-S values in the NSCS and north Pacific subsurface water, implying that the outer sea water gradually mixes with the South China Sea water after passing through the Luzon Strait. Finally, our results show that the factors play an important role in the appearance and distribution of the anomalously high salinity at the subsurface salinity maximum, including the strength of the Kuroshio intrusion, the local wind stress curl and the anticyclonic eddy shedding from the loop current.

Keywords: salinity maximum; anomalously high salinity; Kuroshio intrusion; northern South China Sea; Argo



Citation: Shen, H.; Li, L.; Li, J.; He, Z.; Xia, Y. The Seasonal Variation of the Anomalously High Salinity at Subsurface Salinity Maximum in Northern South China Sea from Argo Data. *J. Mar. Sci. Eng.* **2021**, *9*, 227. <https://doi.org/10.3390/jmse9020227>

Academic Editor: Yannis N. Krestenitis

Received: 27 January 2021
Accepted: 17 February 2021
Published: 20 February 2021

Publisher's Note: MDPI stays neutral with regard to jurisdictional claims in published maps and institutional affiliations.



Copyright: © 2021 by the authors. Licensee MDPI, Basel, Switzerland. This article is an open access article distributed under the terms and conditions of the Creative Commons Attribution (CC BY) license (<https://creativecommons.org/licenses/by/4.0/>).

1. Introduction

The subsurface salinity change patterns provide further indications of an intensified water cycle, including an accentuation of the upper layer salinity contrast between the upper thermocline salinity maximum and the lower thermocline salinity minimum [1,2]. The salinity dynamics in the northern South China Sea (NSCS, 15–21° N, 105–121° E) play an important role in the water cycle between the SCS and North Pacific Tropic ocean (Figure 1). The salinity dynamics, especially at the maximum and minimum layer in this region, have attracted much interest from researchers worldwide, for the maximum and minimum

salinity of the subsurface and intermediate waters are good tracers for delineating the Kuroshio and SCS waters [3].

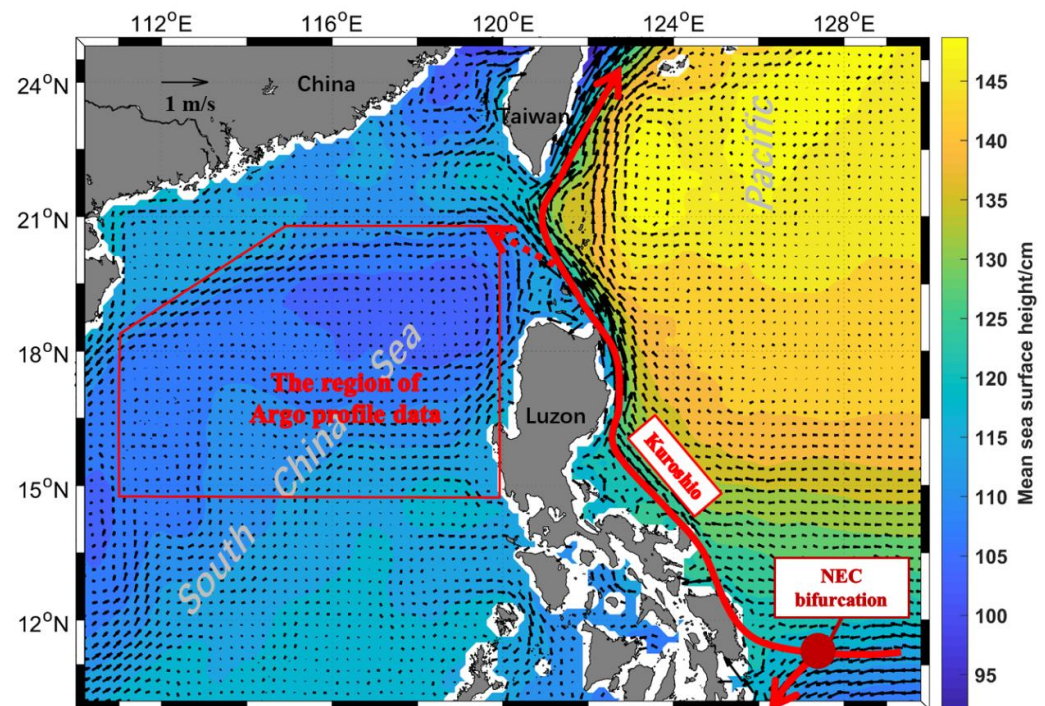


Figure 1. Mean sea surface height (SSH) (cm) and the corresponding surface geostrophic currents (m s^{-1}) derived from 25-year (1993–2018) satellite altimeter data. Red solid lines represent a schematic of the current system. Red box is the research area of Argo profile data. NEC bifurcation is the bifurcation of the North Equatorial Current

Over the past few decades, much work has focused on the Kuroshio intrusion (KI), a water exchange through the Luzon Strait. This work has shown that the salinity in the South China Sea (SCS) reaches an equilibrium state under five constraints, including the Kuroshio intrusion, transports through the three-secondary strait, the downward mixing of freshwater, horizontal mixing induced by mesoscale eddies, and forcing by the local monsoonal winds [4–8]. In contrast with the subsurface water in the NSCS, the Kuroshio water is characterized by higher temperature and salinity, and the depth of the salinity maximum in the Philippine Sea is considerably deeper. Thus, analysis of water masses on pressure surfaces may not be especially appropriate for the region close to the Luzon Strait. Accordingly, the patterns of the NSCS subsurface high-salinity-maximum change are often used as an indicator for changes in the KI [9,10]. The authors in [9] traced the high-salinity North Pacific Tropical Water (NPTW) in the SCS by the waters of the salinity maximum on the density surface between 23.5 and 25.5 kg/m^3 and investigated the distribution of NPTW in the SCS by the location of the 34.6 psu isohaline, based on historical hydrographic data. The authors in [8] used an eddy-resolving regional ocean model to show that the subsurface salinity maximum of the SCS is mainly affected by the SCS throughflow and freshwater flux. However, due to the lack of high-quality and long-term observations, most previous studies have considered only the mean state of waters around the salinity-maximum layer in the NSCS.

More recently, with the improvement of exploration technology, the long-term variability of subsurface salinity [11–13] and the high-resolution observations around the KI, or eddies from the underwater gliders, and Argo have been studied extensively [14–17]. The study in [13] investigated the decadal and long-term variability of subsurface salinity by using a unique in situ dataset and showed that the key factors controlling variations in subsurface salinity are advection driven by the Luzon Strait transport and the vertical entrainment from the mixed layer. The study in [16] argued that the high salinity in the

upper layer of an anticyclonic eddy was more similar to that of the northwestern Pacific Ocean than the northern South China Sea, reflecting Kuroshio intrusion with anticyclonic eddy shedding from the loop current. Although many studies have presented a definition of the subsurface salinity maximum in the NSCS, most have been based on incidental observations from drifters, moorings, autonomous profilers, and shipboard surveys. Consequently, the lack of high-resolution observations has limited our understanding of the anomalously high salinity (>34.65 psu, H-Smax) at the subsurface salinity-maximum layer, which frequently and widely appears in the NSCS. Therefore, it is of scientific and practical value to investigate the sources and distribution characteristics of the anomalously high salinity at the subsurface salinity maximum.

Over the past few years, the Argo program [18,19] has extended its core mission to cover the marginal seas worldwide, and more profiling floats have been launched in the SCS. The Argo-float-derived observations of temperature and salinity provide data for studying the anomalously high salinity of the NSCS. The motivation for this study was to reveal the characteristics of the anomalously high subsurface salinity in the northern South China Sea and the contributions of the controlling factors (e.g., the KI and anticyclonic eddies) to the subsurface salinity anomaly by using Argo-float-derived observations.

Section 2 of this paper describes the data and methodology. Section 3 reports the characteristics of the subsurface salinity maximum and the anomalously high salinity based on Argo data (2006–2019) in the NSCS. Section 4 discusses the effect of possible factors on the anomalously high salinity. Finally, the conclusion and discussion are presented in Section 5.

2. Data and Methodology

2.1. Argo Temperature and Salinity Data

The Argo program in the NSCS started in 2013. A total of 2344 temperature–salinity (T-S) profiles were obtained from the Global Argo Dataset Index and Query System (Version 1.0), which spatially span 15–21° N to 111–121° E and temporally cover 2000 to 2012. Meanwhile, about 3633 T-S profiles from 2013 to 2019 were downloaded from the China Argo Real-time Data Center (CARD) (<http://www.argo.org.cn/> (accessed on 18 February 2021)). After quality control treatments and screening out erroneous data (the number of data between 23.0 and 25.5 σ_θ being less than 5, and the vertical change in data being more than 3 psu/5 m), approximately 5400 T-S profiles were retained and used for this study (Figure 2). Among these, the data beyond 18° N were more than 40% in all the data, and they were evenly distributed in each month, which was suitable for the study in this paper (Figure 2b,c). All the salinities were found to be consistent with each other below 5 °C, indicating the reliability of these Argo observations (Figure 7a).

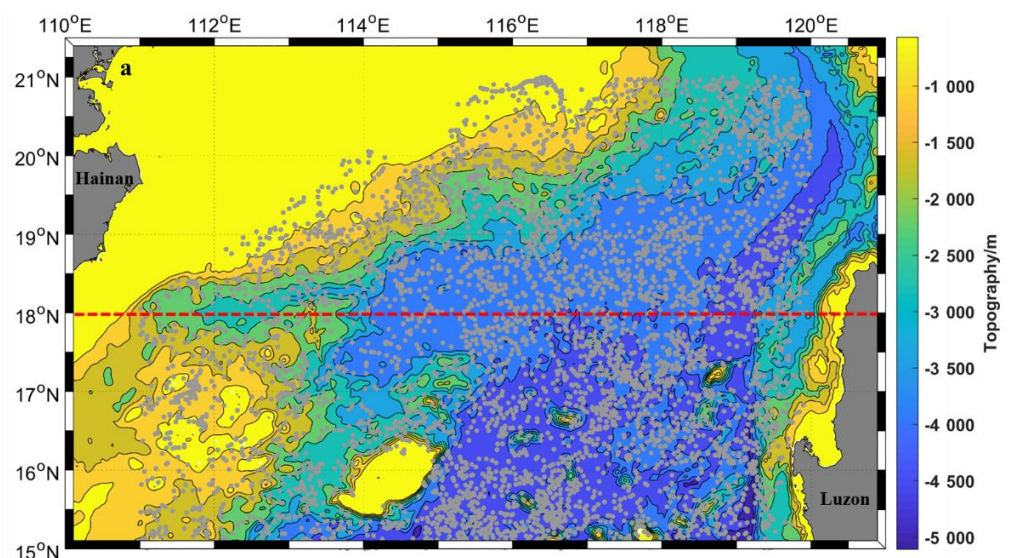


Figure 2. Cont.

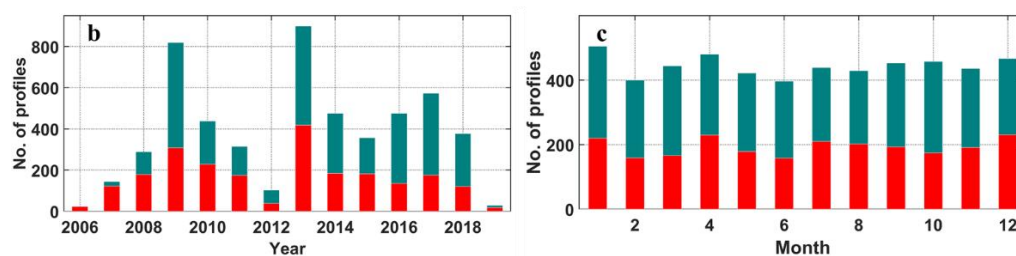


Figure 2. (a) Station map of Argo float profile data (grey dots) in the northern South China Sea (NSCS). Background color indicates bottom topography. (b) Temporal distribution of the count of Argo profile data in each year. Green bars denote the total dataset, and red bars, only the data north of 18° N. (c) Temporal distribution of the count of Argo profile data in each month. Green bars denote the total dataset, and red bars, only the data north of 18° N.

2.2. Altimetry Dataset

The Climatology of Global Gridded Sea Level Anomalies data (SLA, with $1/4^{\circ}$ spatial resolution) and mean dynamic topography data (MDT-clS18, with $1/8^{\circ}$ spatial resolution) provided by Archiving, Validation, and Interpretation of Satellite Oceanographic Data (AVISO; <https://www.aviso.altimetry.fr> (accessed on 18 February 2021)) are used to calculate the SSH and the bifurcation of the North Equatorial Current (NECB). The SSH here is the sum of the SLA and a new version of MDT, which had been computed for the global ocean using a similar method as described in Rio and Hernandez [20–22].

The anticyclonic mesoscale eddies and their parameters, such as position, radius and amplitude, in the NSCS were traced and identified using the AVISO mesoscale eddy trajectory atlas product, which was detected from the multi-mission altimetry data for each day from January 1993 to January 2017 [23–25].

2.3. Wind Data

The monthly sea surface 10 m wind data used in this study were taken from NCEP-DOE Reanalysis 2 (Climatology) based on the widely used NCEP/National Center for Atmospheric Research (NCAR) Reanalysis, which has a spatial resolution of 2.5° . NCEP-DOE Reanalysis 2 is an improved version of the NCEP Reanalysis I model that has fixed errors and updated the parameterizations of physical processes [26].

2.4. Computation and Differentiation of the Subsurface Salinity Maximum

The Argo profiles were interpolated to a vertical uniform grid with a resolution of 5 dbar, from 0 to 1500 dbar, using a piecewise cubic Hermite interpolating polynomial (PCHIP). The salinity maximum and its location were calculated from the interpolated data (Figure 3). Then, the results were classified by season to describe the seasonal variation (January–March for winter, April–June for spring, July–September for summer, and October–December for fall).

According to Figure 7c, salinity more than 34.65 (probability is about 0.25, H-Smax) and salinity more than 34.75 (probability is about 0.05 and is 4 times larger than the result of normal distribution; higher H-Smax) were selected as the tipping points to differentiate the salinity values.

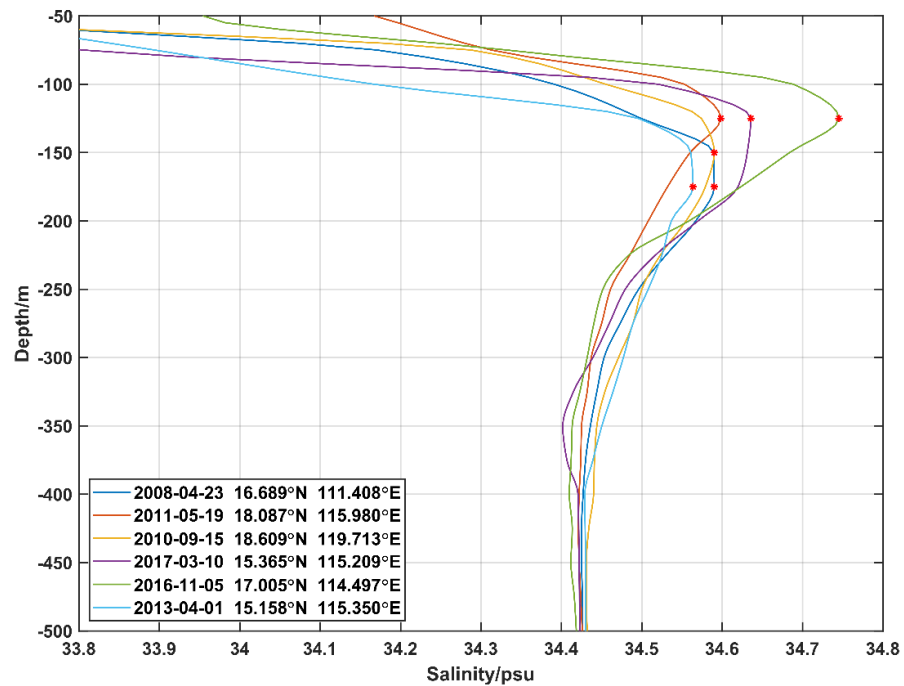


Figure 3. Salinity profiles in the NSCS (red dots are the subsurface salinity maximum).

3. Results

3.1. Distribution Characteristics of the Subsurface Salinity Maximum and Its Depth in the NSCS

The spatial distribution of the subsurface salinity maximum in Figure 4a shows that the values covering the NSCS stayed in the range of 34.45–34.65 psu during most of the observation time, which is consistent with previous studies [9,13]. High salinity values (>34.65 psu) were captured in some profiles located near the Philippine Islands. More anomalously high salinity values at the subsurface salinity maximum occurred in the northeast than in the southwest.

The salinity maximum in the NSCS generally occurred at depths ranging from 100 to 200 m (Figure 4b). Similarly, more subsurface salinity-maximum values occurred at depths of less than 80 m in the northeast than in the south of the NSCS. The distribution of these profiles implies that the outer sea water may gradually mix with the South China Sea water after passing through the Luzon Strait.

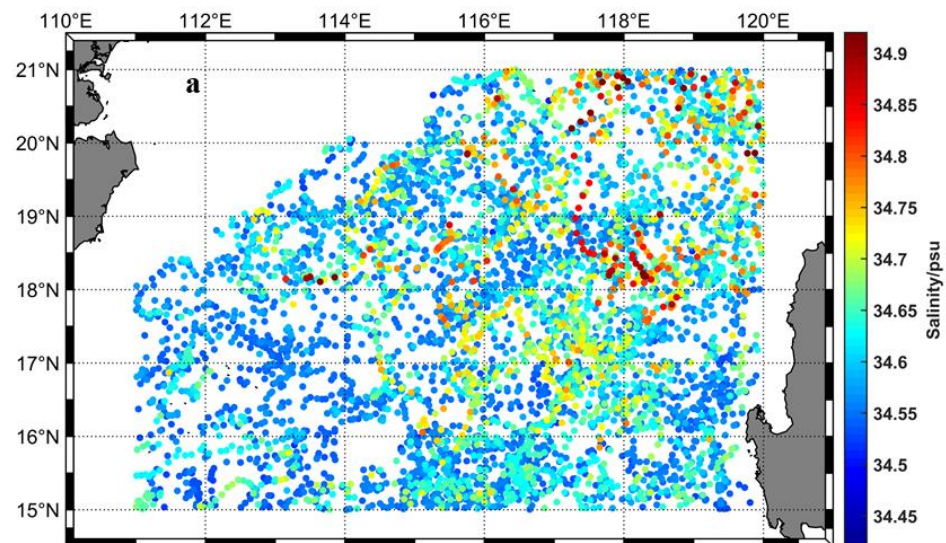


Figure 4. Cont.

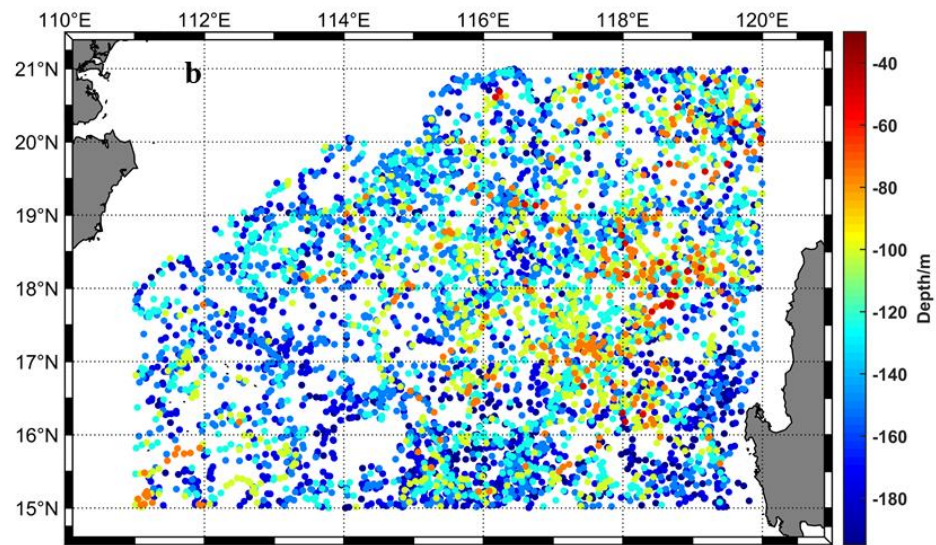


Figure 4. Scatter plots of (a) salinity in psu, and (b) depth in meters in the subsurface salinity-maximum layer from 2006 to 2019 in the NSCS.

Figure 5 shows the seasonal variation of the salinity maximum. The anomalously high salinity values (>34.75 psu) at the subsurface salinity maximum were more in winter than in summer. Some anomalously high salinity values at the subsurface salinity maximum occurred to the south of 17° N in winter, while appearing sporadically near 18° N in summer. According to Figure 6, the depth of the subsurface salinity maximum also shows a significant seasonal signal. The salinity maximum was usually observed at the shallow layer in winter, followed by spring and fall. By contrast, most of the subsurface salinity-maximum values appeared in deeper water of more than 120 m, especially in the southeast in summer.

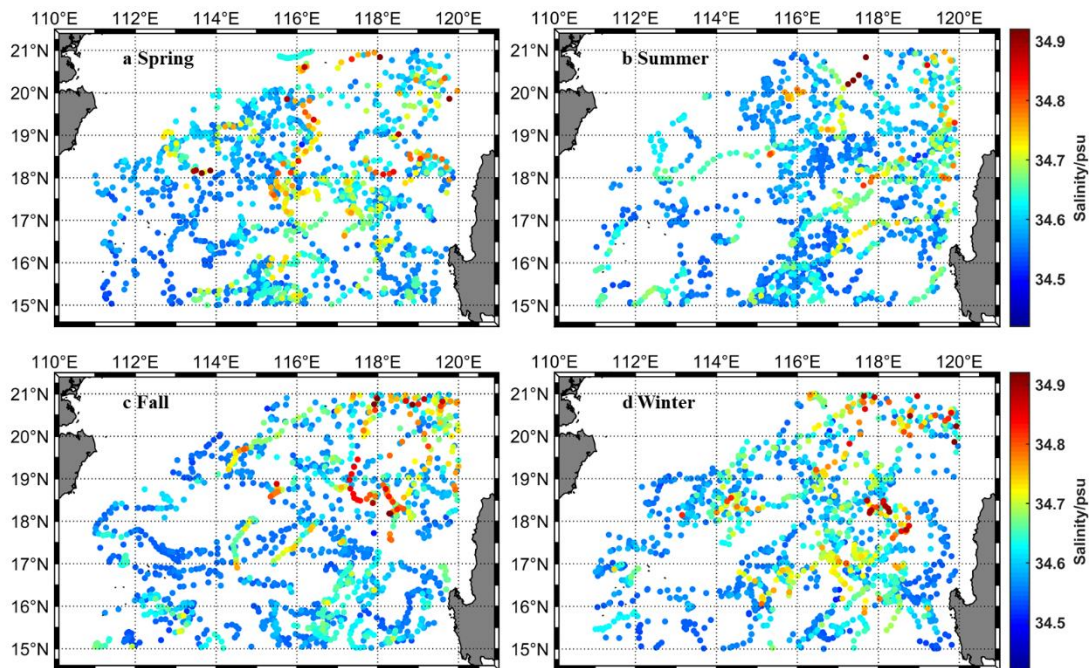


Figure 5. Seasonal variation of the salinity (psu) in the salinity-maximum layer.

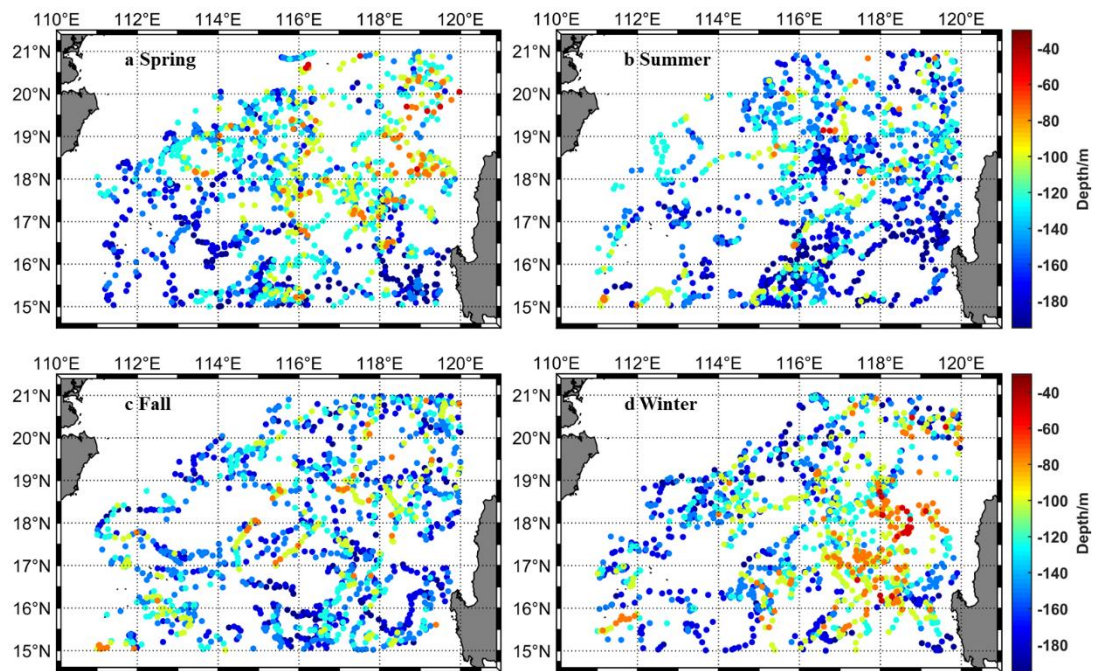


Figure 6. Seasonal variation of the depth (meters) in the salinity-maximum layer.

3.2. Anomalous High Subsurface Salinity

The results as mentioned above show that anomalously high salinity at the subsurface salinity maximum (salinity > 34.65 psu, H-Smax) frequently occurred in the NSCS, especially the area near the Luzon Strait. Therefore, it is of scientific and practical value to investigate the sources and distribution characteristics of the anomalously high salinity at the subsurface salinity maximum. The NSCS waters above the intermediate layer contain four well-defined water masses (T-S diagram in Figure 7a): the North Pacific Tropical Water (NPTW), low-salinity North Pacific Intermediate Water (NPIW), North Pacific Surface Water (NPSW) and NSCS Warm Water (NSCSWW). In Figure 7a, all the red dots (salinity maximum data) range between 34.45 and 34.65 (the dashed curves are isopycnals with σ_θ values (kg/m^3) denoted). The T-S diagrams from the Argo vertical profiles (2006–2019) in the NSCS (Figure 7a) show that the T-S values at the salinity-maximum layer appeared in the NPTW (North Pacific Tropical Water) zone, indicating that the subsurface waters share characteristics with the North Pacific Tropical Water. In addition, a portion of the salinity maximum was distributed in the H-Smax zone, indicating that part of the subsurface water was characterized by high temperature ($T > 18^\circ\text{C}$) and high salinity data (salinity > 34.65 psu). As shown in Figure 7b, the statistical result of the salinity of the salinity-maximum data was not a Gaussian distribution. The skewness of the data was 1.477, implying that anomalously high salinity occasionally appeared in the NSCS. The mode of the salinity was 34.55 psu, which accounted for more than 13% of the total. The data greater than the mode accounted for 75%. The number of salinity-maximum data with salinity larger than 34.65 psu accounted for about 23% of the total salinity-maximum data [3].

To investigate the source of the H-Smax, the water masses in the east of the Luzon Strait and the NSCS were further analyzed. A prominent feature of water masses is that, at any given depth in the mixed and subsurface layers, the NPTW (Figure 8, green dotted curve) is warmer and saltier than the NSCS water (Figure 8, blue dotted curve). The subsurface T-S values of the profiles containing the H-Smax were mainly between the mean T-S values in the NSCS and the north Pacific, which indicates that H-Smax water masses have the properties of NSCS water and NPTW. We can suggest that this water originated from the western Pacific and was likely to intrude into the NSCS through the Luzon Strait during the observation time. The salinity of intermediate water (below $26\sigma_\theta$) evenly

distributes around the mean T-S values in the NSCS because of the negligible invasion of open sea, which is consistent with the results of previous studies [9,10,30,31].

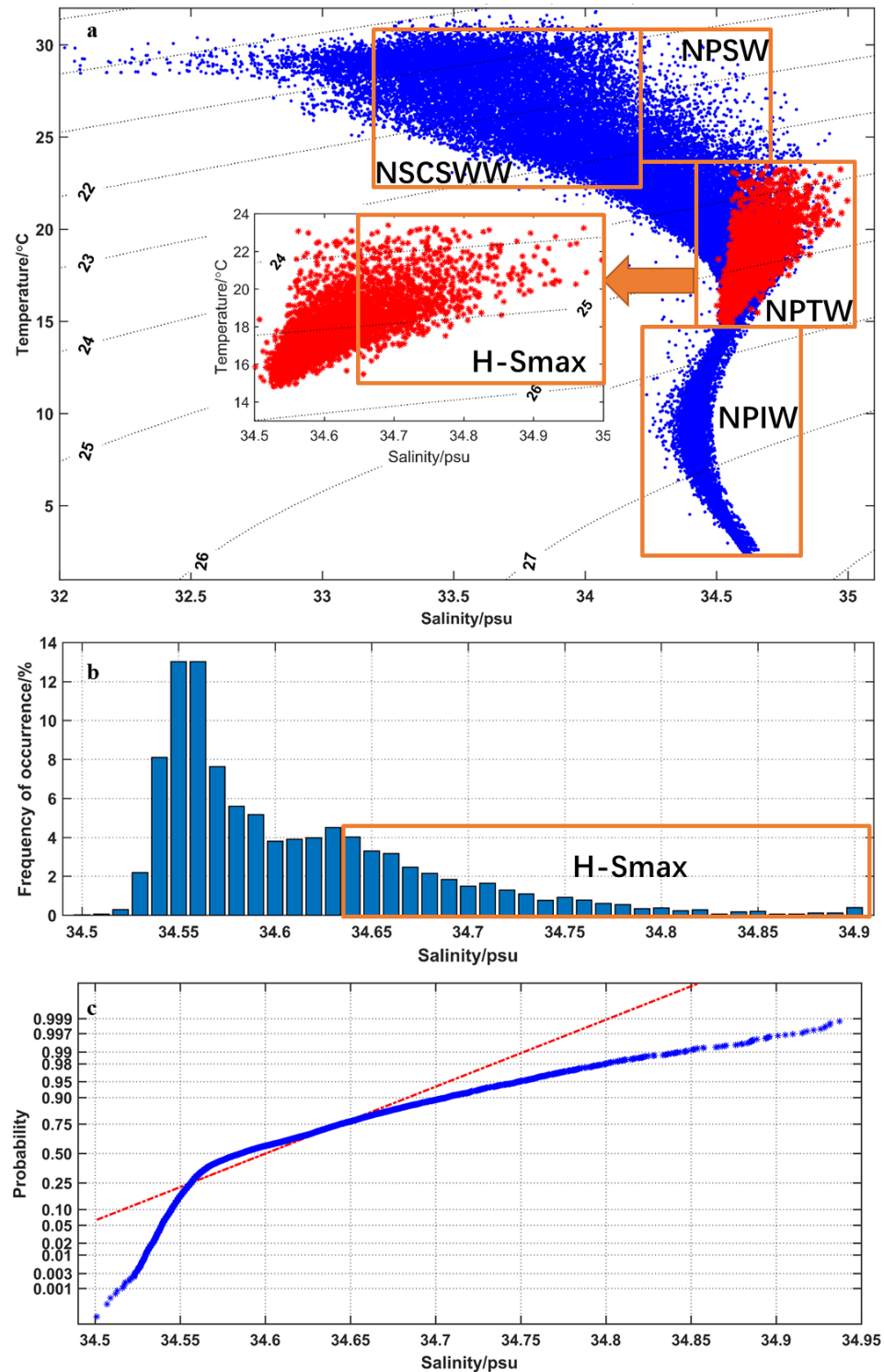


Figure 7. (a) T-S diagrams from Argo vertical profiles (2006–2019) in the NSCS. The dashed curves are isopycnals with σ_θ values (kg/m^3) denoted. The blue dots and red dots stand for all Argo profiles and the salinity-maximum data, respectively. The definitions of different water masses were based on [3,9,13,27–29]. NPTW: North Pacific Tropical Water; NPIW: low-salinity North Pacific Intermediate Water; NPSW: North Pacific Surface Water; NSCSWW: NSCS Warm Water; H-Smax: anomalously high subsurface salinity water in the NSCS. (b) The frequency histogram of the salinity-maximum data by salinity. (c) The normal probability plot of the salinity-maximum data by salinity.

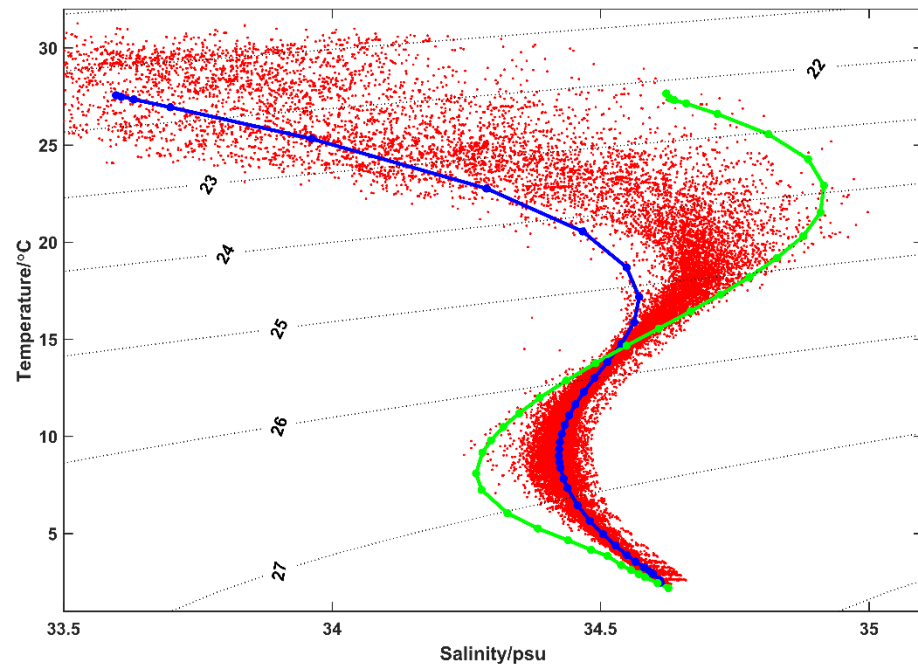


Figure 8. The T-S diagram of NPW, NSCS, and the H-Smax water. The blue and green dotted lines represent mean T-S values in NSCS and NPTW from Argo profiles (NSCS, 15–21° N 111–121° E; NPTW, 18–22° N 121–123° E), respectively, and the red dots denote T-S of the H-Smax water.

The distribution of the H-Smax in the NSCS shows significant spatial differences (Figure 9). The frequency of the H-Smax in the northeast and southeast of the NSCS was generally higher than that in the northwest and southwest of the NSCS. The occurrence frequency of the higher H-Smax (>34.75) in the northeastern region was much larger than that in other regions, while the highest frequency of the lower H-Smax (34.65–34.7) occurred in the southeastern region, and could reach 17% in total. In the northwestern region, the frequency of the higher H-Smax was second only to that in the northeast, indicating that a small number of high-salinity seawater masses can spread westward near the shelf slope after entering the Luzon Strait. The frequency of the salinity Smax in the southwestern region is the smallest, because the NPTW that intrudes into the NSCS hardly reaches this place before mixing in the NSCS [3].

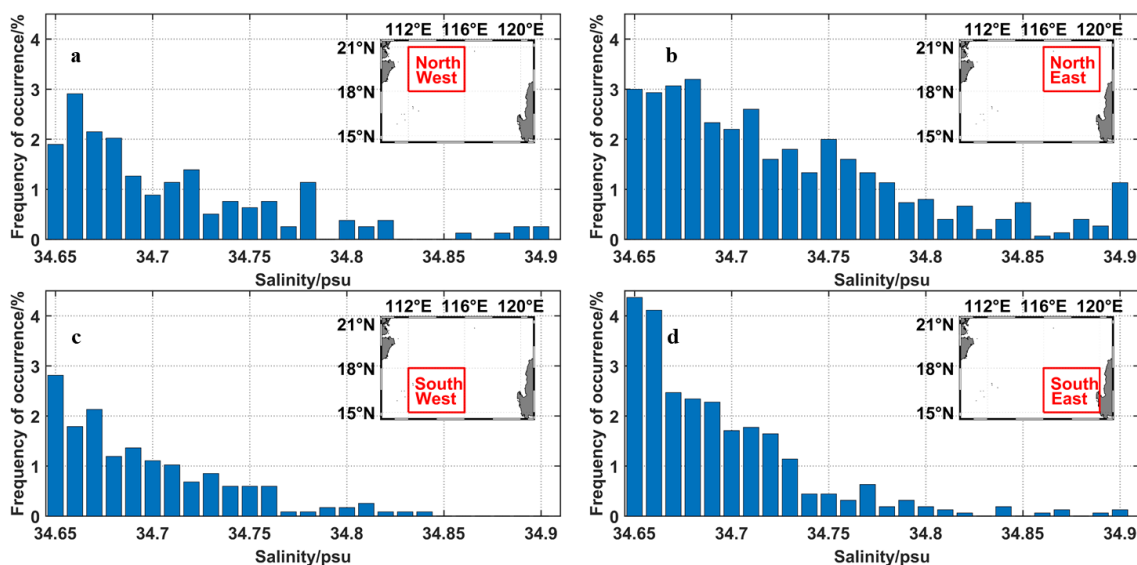


Figure 9. The frequency histogram of the salinity-maximum data by salinity (>34.65) in the different areas of the NSCS.

4. Discussion

On the mechanism of the subsurface salinity-maximum changes in the NSCS, studies have revealed that horizontal advection and vertical entrainment are key factors [12,13,32]. The former is favorable for subsurface salinification, and the latter is the source of subsurface freshening. To understand the variations in H-Smax, we investigated the main underlying processes that modify the subsurface water.

4.1. Effects of the Strength of KI on Anomally High Subsurface Salinity

Previous studies [33,34] pointed out that the strength of the Kuroshio transport to the SCS was related to the bifurcation of the North Equatorial Current (NECB) near the coast of the Philippines. A stronger Mindanao Dome and a weaker Kuroshio transport would be formed near the east coast of the Philippines when the bifurcation of the North Equatorial Current moved northward [35,36]. When the Kuroshio transport weakened, the meridional advection of the potential vorticity was not strong enough to overpower the β effect, and so the boundary current could switch into the “gap penetrating” regime easily [37]. This behavior was analogous to the well-known teapot effect [38]. The proxy bifurcation latitude of the North Equatorial Current ($NECB_{lat}$) from SSH data was calculated according to [33]:

$$NECB_{lat} = 11.9 - 0.13 \times h'(t) \tag{1}$$

where $h'(t)$ is the monthly SSH anomaly value (in cm) averaged in the 12–14° N and 127–130° E box.

As shown in Figure 10, the occurrence frequency of the H-Smax was consistent with the latitudinal variation of the NECB, and the correlation coefficient reached 0.92. The occurrence frequency of the H-Smax was decreasing as the NECB moved southward from spring to summer. In August, when the latitude of the NECB was lower than 11.5° N, the occurrence probability of the H-Smax was lower than 21%. By contrast, the occurrence frequency of the H-Smax was increasing as the NECB moved northward from autumn to winter. In December, when the $NECB_{lat}$ was higher than 12.5° N, the occurrence probability of the H-Smax was higher than 26%. The corresponding relationship between the occurrence frequency of the H-Smax and the latitude location of the NECB shows that the occurrence frequency of the H-Smax is positively correlated with the strength of the KI.

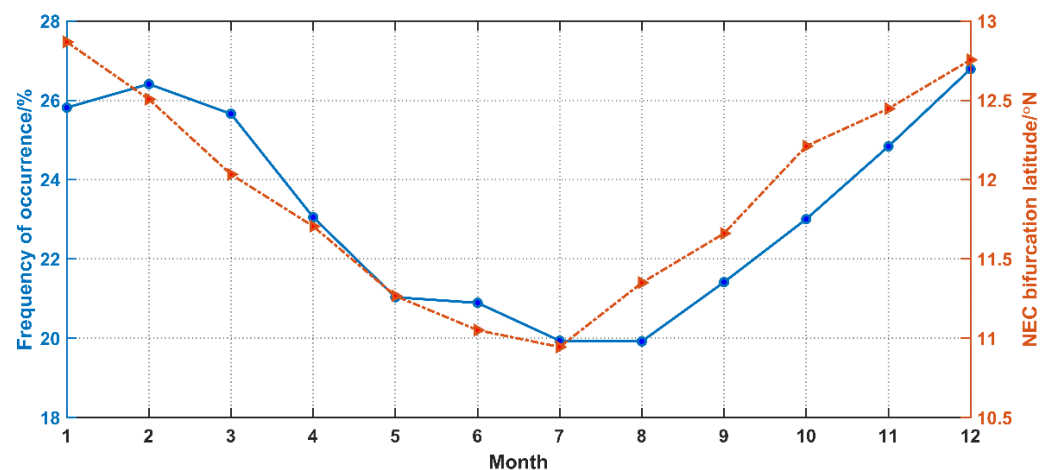


Figure 10. Frequency of H-Smax occurrence (blue line) and NEC bifurcation latitude (red line) as a function of calendar month.

4.2. Effects of Local Wind Stress Curl on Anomally High Subsurface Salinity

Ekman transport and Ekman pumping induced by wind stress curl play an important role in the seasonal variation of the Kuroshio intrusion [3] and vertical entrainment [39]. Ekman transport contributed to the seasonal variation (stronger in winter and weaker in summer) of the Kuroshio intrusion [3], accounting for less than 10% of the total Luzon

Strait transport [40]. During the Ekman pumping process, wind stress curl generated divergence, forcing an upward water movement [39], freshening the subsurface water and lifting the thermoclines.

The wind stress curl was calculated from surface U/V-Wind data obtained from NCEP-DOE Reanalysis 2 (Climatology, monthly long-term means; this project used a state-of-the-art analysis/forecast system to perform data assimilation using past data from 1948 to the present). Figure 11 shows the corresponding relationship between the wind stress curl and depth in the salinity-maximum layer near the Luzon Strait. A positive wind stress curl was found on the west/east side of the NSCS in summer/winter (Figure 11a,b). The wind stress curl in June was the smallest, and then, it increased month by month and reached the largest magnitude in December. The depth in the salinity-maximum layer began to change 1–2 months later than the change in wind stress, and it decreased from August to January in the next year (Figure 11c). This may explain that the associated changes in the wind stress curl cause the shallower depth in the subsurface salinity maximum on the west coast of Luzon in winter.

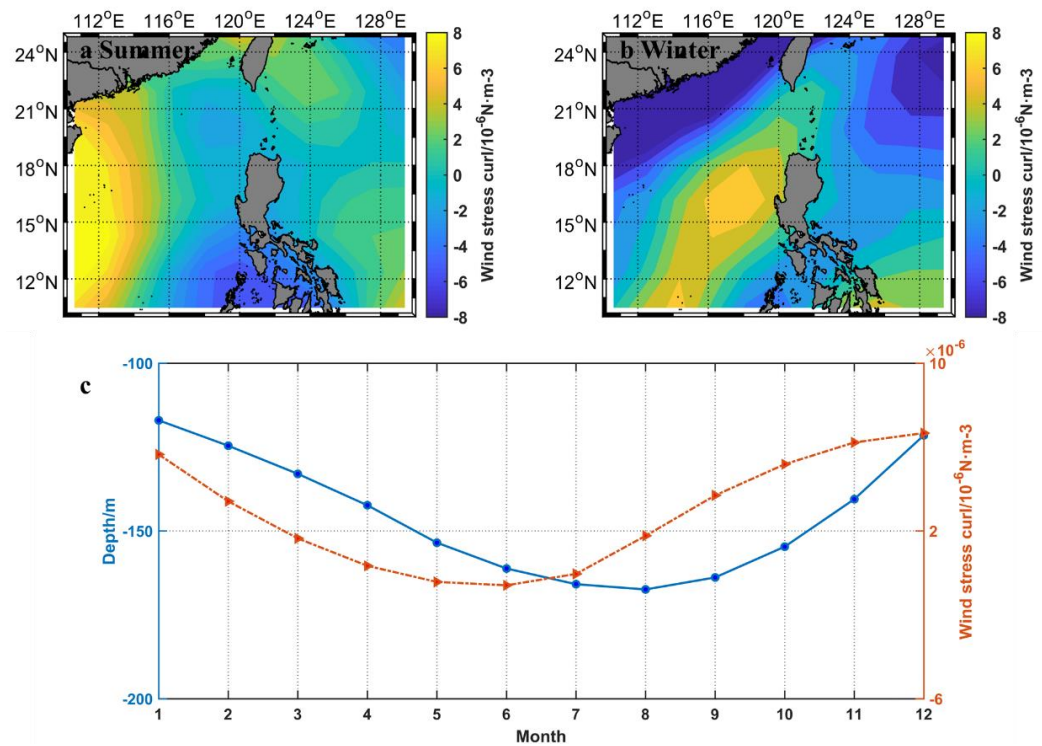


Figure 11. Mean wind stress curl derived from the National Centers for Environmental Prediction (NCEP) monthly Climatology Data: (a) Summer (June–August); (b) Winter (December–February). (c) Depth in the salinity-maximum layer (blue line, averaged in the 14–19° N and 115–120° E box) and wind stress curl (red line) as a function of calendar month.

4.3. Effects of Anticyclonic Eddies Shedding from the Loop Current on Anomalously High Subsurface Salinity

Subsurface salinity is affected by the rotation of mesoscale eddies and the eddy-induced transport. The upwelling/downwelling inside a cyclonic/anticyclonic eddy causes the upward/downward transport of deep cold water/warm surface water, resulting in subsurface salinity changes [16]. Meanwhile, unlike the large-scale circulation that transports fluids and their properties continuously, mesoscale eddies can trap fluid parcels within the eddy core and transport them discretely [41]. As a result, anticyclonic eddies, like giant buckets, could carry the NPTW, characterized by high temperature and salinity, to the NSCS. The corresponding annual-mean transport caused by the Kuroshio Loop Current eddy shedding reaches 0.24–0.38 Sv ($1 \text{ Sv} = 10^6 \text{ m}^3\text{s}^{-1}$), accounting for 6.8%–10.8% of the upper-layer Luzon Strait transport [17].

The anticyclonic eddies shed from the Kuroshio loop have been distinguished because the origins and paths of each eddy can be obtained from AVISO data. The number of days from the anticyclone originating from Kuroshio looping (starting position: latitude $>18^\circ$ N, longitude $>119.5^\circ$ E) to occurring in the NSCS were counted according to AVISO eddy trajectory data for the past two decades (Figure 12). Statistics were performed once a day, and only the occurrence area containing the center position of the eddy was counted. In winter, the anticyclonic eddy was present on 1192 out of 2070 days in the NSCS. The number of anticyclonic eddies is the largest in the northwestern area of Luzon Island, and some anticyclones can propagate along the shelf slope to the southeast of Hainan Island, indicating that high-salt water occasionally occurred near the northern shelf slope of the NSCS. In summer, an anticyclonic eddy was present on 493 out of 2116 days in the NSCS, mostly being located near the Luzon Strait. The total number and the distribution areas of the anticyclonic eddies were less than in winter. Comparing the results of Figure 5, we can conclude that the coverage area and seasonal variation of the anticyclone and H-Smax are consistent.

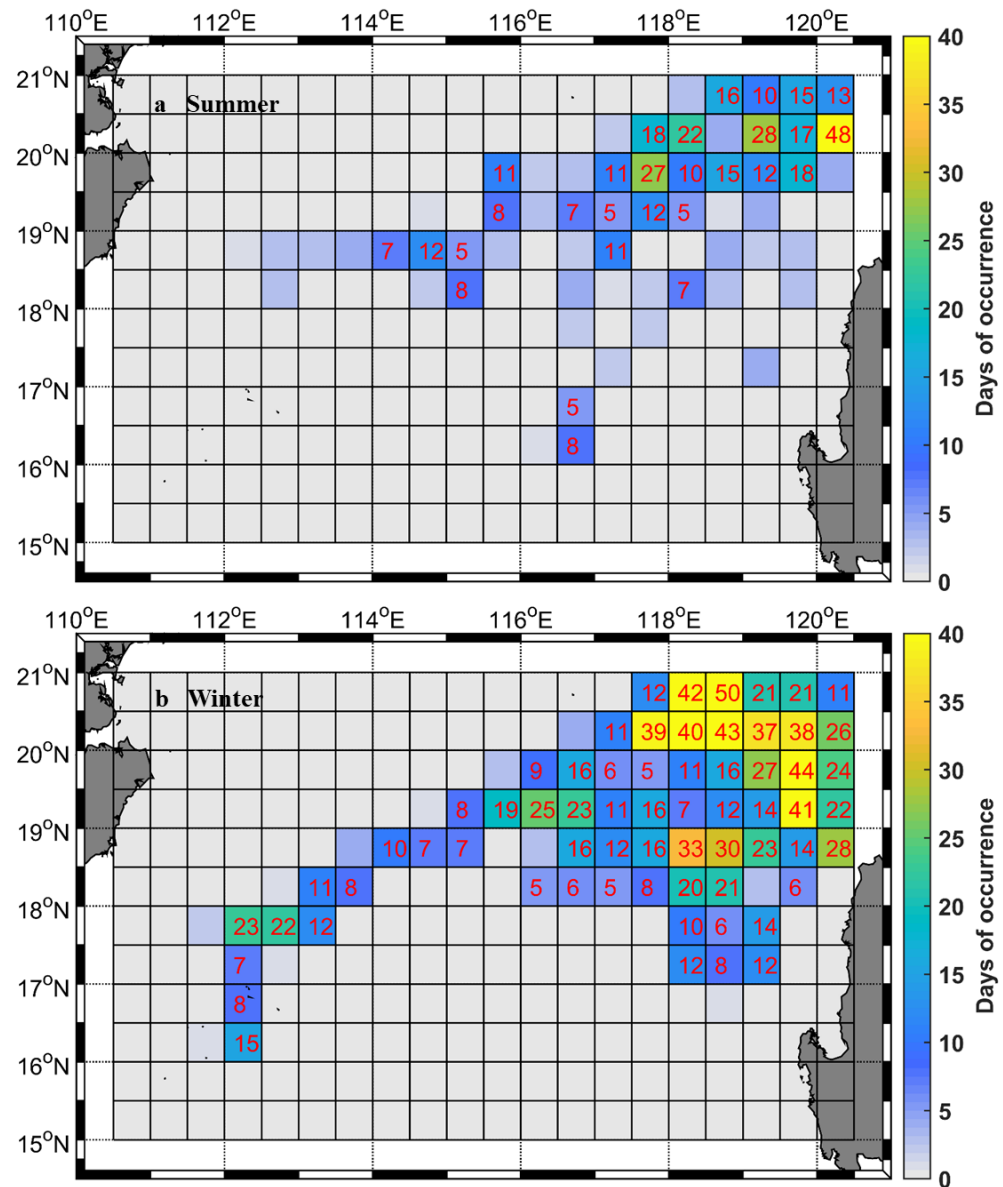


Figure 12. The spatial patterns of eddy occurrence (existence days ≥ 5) in the NSCS from 1993 to 2017. (a) Summer (June–August); (b) Winter (December–February).

5. Conclusions

In this study, the characteristics of the anomalously high subsurface salinity in the NSCS and possible factors controlling this change were explored. The subsurface salinity maximum and its depth in the north South China Sea (NSCS) were calculated from 2006–2019 Argo data. The high salinity located at the shallow depth (<80 m) of the subsurface salinity maximum was more likely to appear in the northeast than in the south of the NSCS. The salinity and depth of the subsurface salinity maximum showed significant seasonal signals. The anomalously high salinity at the subsurface salinity maximum accounted for about 23% of the total salinity-maximum values in the NSCS, especially near the Luzon Strait. In winter, the anomalously high salinity at the shallow subsurface salinity maximum can extend to the south of 17° N, while in summer, it rarely reached as far as 18° N and tended to locate in deeper waters. From the T-S analysis, we found that the subsurface salinity of the Kuroshio water was notably higher than that of the NSCS water, and the water mass of the H-Smax manifests the properties of the NSCS and NPTW.

The strength of the Kuroshio intrusion, the local wind stress curl and the anticyclonic eddies shedding from the loop current contribute to the changes in the H-Smax. The occurrence frequency of the H-Smax was positively correlated with the strength of the KI. The occurrence frequency of the H-Smax was decreasing (increasing) and the NECB was moving southward (northward) from the spring to the summer (the autumn to the winter). The vertical entrainment induced by the positive wind stress curl freshened the subsurface water and lifted the salinity maximum on the west coast of Luzon. It explained the high correlation between the shallower depth of the anomalously high salinity and the distribution of the positive curl in winter. The occurrence frequencies of the H-Smax and the anticyclonic eddies near the Luzon Strait were highly correlated, showing a positive effect of anticyclonic eddies on the H-Smax. Note that our understanding about the variability in the subsurface salinity maximum has been limited by the lack of long-term observations. Although Argo deployment in the NSCS started in 2006, the number of operational floats has never been sufficient for monitoring the variability in the thermohaline structure over whole region, where the water masses are evidently influenced by the NPTW through the Luzon Strait. Therefore, it is appropriate to conduct multiplatform 4-D (latitude, longitude, depth and time) observational surveys with efficient means (e.g., Argo and underwater gliders) in the NSCS, focusing on the T-S profiles at a large spatiotemporal scale.

Author Contributions: Conceptualization, H.S., Z.H. and Y.X.; Data curation, H.S.; Formal analysis, L.L.; Funding acquisition, L.L., J.L. and Z.H.; Investigation, H.S.; Project administration, J.L. and Z.H.; Supervision, Y.X.; Validation, H.S. and L.L.; Visualization, H.S.; Writing—original draft, H.S.; Writing—review & editing, L.L., Z.H. and Y.X. All authors have read and agreed to the published version of the manuscript.

Funding: This study was supported by the National Key Research and Development Program of China (Grant No. 2016YFC1400100 and 2017YFC0305905), and the NSFC-Zhejiang Joint Fund for the Integration of Industrialization and Informatization (U1709204).

Institutional Review Board Statement: Not applicable.

Informed Consent Statement: Not applicable.

Data Availability Statement: We are grateful for the Argo T-S profiles provided by the China Argo Real-time Data Center (CARD) (<http://www.argo.org.cn/> (accessed on 18 February 2021)), The monthly sea surface 10 m wind data were taken from NCEP-DOE Reanalysis 2 (Climatology) and sea level anomaly data and the mesoscale eddy trajectory data provided by Archiving, Validation, and Interpretation of Satellite Oceanographic Data (AVISO; <https://www.argo.altimetry.fr> (accessed on 18 February 2021)).

Acknowledgments: We would like to thank Dongping Wang for valuable comments.

Conflicts of Interest: The authors declare no conflict of interest.

References

1. Helm, K.P.; Bindoff, N.L.; Church, J.A. Changes in the global hydrological-cycle inferred from ocean salinity. *Geophys. Res. Lett.* **2010**, *37*, L18701. [[CrossRef](#)]
2. Skliris, N.; Marsh, R.; Josey, S.A.; Good, S.A.; Liu, C.; Allan, R.P. Salinity changes in the World Ocean since 1950 in relation to changing surface freshwater fluxes. *Clim. Dyn.* **2014**, *43*, 709–736. [[CrossRef](#)]
3. Nan, F.; Xue, H.; Yu, F. Kuroshio intrusion into the South China Sea: A review. *Prog. Oceanogr.* **2015**, *137*, 314–333. [[CrossRef](#)]
4. Hsin, Y.C. Multidecadal variations of the surface Kuroshio between 1950s and 2000s and its impacts on surrounding waters. *J. Geophys. Res. Oceans* **2015**, *120*, 1792–1808. [[CrossRef](#)]
5. Li, L.; Qu, T. Thermohaline circulation in the deep South China Sea basin inferred from oxygen distributions. *J. Geophys. Res. Oceans* **2006**, *111*, C05017. [[CrossRef](#)]
6. Shaw, P.T. The seasonal variation of the intrusion of the Philippine Sea water into the South China Sea. *J. Geophys. Res. Oceans* **1991**, *96*, 821–827. [[CrossRef](#)]
7. Tsui, I.F.; Wu, C.R. Variability analysis of Kuroshio intrusion through Luzon Strait using growing hierarchical self-organizing map. *Ocean Dyn.* **2012**, *62*, 1187–1194. [[CrossRef](#)]
8. Yu, Z.; McCreary, J.P.; Yaremchuk, M.; Furue, R. Subsurface Salinity Balance in the South China Sea*. *J. Phys. Oceanogr.* **2008**, *38*, 527–539. [[CrossRef](#)]
9. Qu, T.; Mitsudera, H.; Yamagata, T. Intrusion of the north Pacific waters into the South China Sea. *J. Geophys. Res. Oceans* **2000**, *105*, 6415–6424. [[CrossRef](#)]
10. Zhou, H.; Nan, F.; Shi, M.; Zhou, L.; Guo, P. Characteristics of water exchange in the Luzon Strait during September 2006. *Chin. J. Oceanol. Limnol.* **2009**, *27*, 650–657. [[CrossRef](#)]
11. Goes, M.; Wainer, I.; Signorelli, N. Investigation of the causes of historical changes in the subsurface salinity minimum of the South Atlantic. *J. Geophys. Res. Oceans* **2014**, *119*, 5654–5675. [[CrossRef](#)]
12. Chen, X.; Liu, Z.; Wang, H.; Xu, D.; Wang, L. Significant salinity increase in subsurface waters of the South China Sea during 2016–2017. *Acta Oceanol. Sin.* **2019**, *38*, 51–61. [[CrossRef](#)]
13. Zeng, L.; Wang, D.; Xiu, P.; Shu, Y.; Wang, Q.; Chen, J. Decadal variation and trends in subsurface salinity from 1960 to 2012 in the northern South China Sea. *Geophys. Res. Lett.* **2016**, *43*, 12181–12189. [[CrossRef](#)]
14. Li, G.; Zhang, Y.; Xiao, J.; Song, X.; Abraham, J.; Cheng, L.; Zhu, J. Examining the salinity change in the upper Pacific Ocean during the Argo period. *Clim. Dyn.* **2019**, *53*, 6055–6074. [[CrossRef](#)]
15. Li, S.; Wang, S.; Zhang, F.; Wang, Y. Constructing the three-dimensional structure of an anticyclonic eddy in the South China Sea using multiple underwater gliders. *J. Atmos. Ocean. Technol.* **2019**, *36*, 2449–2470. [[CrossRef](#)]
16. Liu, Z.; Chen, X.; Yu, J.; Xu, D.; Sun, C. Kuroshio intrusion into the South China Sea with an anticyclonic eddy: Evidence from underwater glider observation. *Chin. J. Oceanol. Limnol.* **2019**, *37*, 1469–1480. [[CrossRef](#)]
17. Zhang, Z.; Zhao, W.; Qiu, B.; Tian, J. Anticyclonic eddy sheddings from Kuroshio loop and the accompanying cyclonic eddy in the northeastern South China Sea. *J. Phys. Oceanogr.* **2017**, *47*, 1243–1259. [[CrossRef](#)]
18. Liu, Z.; Wu, X.; Xu, J.; Li, H.; Lu, S.; Sun, C.; Cao, M. China Argo project: Progress in China Argo ocean observations and data applications. *Acta Oceanol. Sin.* **2017**, *36*, 1–11. [[CrossRef](#)]
19. Riser, S.C.; Freeland, H.J.; Roemmich, D.; Wijffels, S.; Jayne, S.R. Fifteen years of ocean observations with the global Argo array. *Nat. Clim. Chang.* **2016**, *6*, 145–153. [[CrossRef](#)]
20. Maximenko, N.; Niiler, P.; Centurioni, L.; Rio, M.; Melnichenko, O.; Chambers, D.; Zlotnicki, V.; Galperin, B. Mean dynamic topography of the ocean derived from satellite and drifting buoy data using three different techniques. *J. Atmos. Ocean. Technol.* **2009**, *26*, 1910–1919. [[CrossRef](#)]
21. Rio, M.H.; Hernandez, F. A mean dynamic topography computed over the world ocean from altimetry, in situ measurements, and a geoid model. *J. Geophys. Res. Oceans* **2004**, *109*, C12032. [[CrossRef](#)]
22. Rio, M.H.; Mulet, S.; Picot, N. Beyond GOCE for the ocean circulation estimate: Synergetic use of altimetry, gravimetry, and in situ data provides new insight into geostrophic and Ekman currents. *Geophys. Res. Lett.* **2014**, *41*, 8918–8925. [[CrossRef](#)]
23. Chelton, D.B.; Schlax, M.G.; Samelson, R.M. Global observations of nonlinear mesoscale eddies. *Prog. Oceanogr.* **2011**, *91*, 167–216. [[CrossRef](#)]
24. Mason, E.; Pascual, A.; McWilliams, J.C. A new sea surface height-based code for oceanic mesoscale eddy tracking. *J. Atmos. Ocean. Technol.* **2014**, *31*, 1181–1188. [[CrossRef](#)]
25. Schlax, M.G.; Chelton, D.B. The “Growing Method” of Eddy Identification and Tracking in Two and Three Dimensions. Ph.D. Thesis, College of Earth, Ocean and Atmospheric Sciences, Oregon State University, Corvallis, OR, USA, 2016.
26. Kanamitsu, M.; Ebisuzaki, W.; Woollen, J.; Yang, S.; Hnilo, J.J.; Fiorino, M.; Potter, G.L. NCEP–DOE AMIP-II Reanalysis (R-2). *Bull. Amer. Meteorol. Soc.* **2002**, *83*, 1631–1644. [[CrossRef](#)]
27. Hu, J.; Kawamura, H.; Hong, H.; Qi, Y. A review on the currents in the South China Sea: Seasonal circulation, South China Sea warm current and Kuroshio intrusion. *J. Oceanogr.* **2000**, *56*, 607–624. [[CrossRef](#)]
28. Su, J. Overview of the South China Sea circulation and its influence on the coastal physical oceanography outside the Pearl River Estuary. *Cont. Shelf Res.* **2004**, *24*, 1745–1760.
29. Wang, Z.; Ren, J.; Xuan, J.; Li, F.; Yang, T.; Guo, Y. Processes controlling the distribution and cycling of dissolved manganese in the northern South China Sea. *Mar. Chem.* **2018**, *204*, 152–162. [[CrossRef](#)]

30. Liu, Y.; Bye, J.A.; You, Y.; Bao, X.; Wu, D. The flushing and exchange of the South China Sea derived from salt and mass conservation. *Deep-Sea Res. Part II-Top. Stud. Oceanogr.* **2010**, *57*, 1212–1220. [[CrossRef](#)]
31. Park, J.; Lim, B. A new perspective on origin of the East Sea Intermediate Water: Observations of Argo floats. *Prog. Oceanogr.* **2018**, *160*, 213–224. [[CrossRef](#)]
32. Nan, F.; Yu, F.; Xue, H.; Zeng, L.; Wang, D.; Yang, S.; Nguyen, K.C. Freshening of the upper ocean in the South China Sea since the early 1990s. *Deep-Sea Res. Part I-Oceanogr. Res. Pap.* **2016**, *118*, 20–29. [[CrossRef](#)]
33. Qiu, B.; Chen, S. Interannual-to-decadal variability in the bifurcation of the North Equatorial Current off the Philippines. *J. Phys. Oceanogr.* **2010**, *40*, 2525–2538. [[CrossRef](#)]
34. Toole, J.M.; Millard, R.C.; Wang, Z.; Pu, S. Observations of the Pacific North Equatorial Current Bifurcation at the Philippine Coast. *J. Phys. Oceanogr.* **1990**, *20*, 307–318. [[CrossRef](#)]
35. Masumoto, Y.; Yamagata, T. Response of the western tropical Pacific to the Asian winter monsoon: The generation of the Mindanao Dome. *J. Phys. Oceanogr.* **1991**, *21*, 1386–1398. [[CrossRef](#)]
36. Tozuka, T.; Kagimoto, T.; Masumoto, Y.; Yamagata, T. Simulated Multiscale Variations in the Western Tropical Pacific: The Mindanao Dome Revisited. *J. Phys. Oceanogr.* **2002**, *32*, 1338–1359. [[CrossRef](#)]
37. Wang, D.; Liu, Q.; Huang, R.; Du, Y.; Qu, T. Interannual variability of the South China Sea throughflow inferred from wind data and an ocean data assimilation product. *Geophys. Res. Lett.* **2006**, *33*, L14605. [[CrossRef](#)]
38. Sheremet, V.A. Hysteresis of a Western Boundary Current Leaping across a Gap. *J. Phys. Oceanogr.* **2001**, *31*, 1247–1259. [[CrossRef](#)]
39. Yan, Y.; Ling, Z.; Chen, C. Winter coastal upwelling off northwest Borneo in the South China Sea. *Acta Oceanol. Sin.* **2015**, *34*, 3–10. [[CrossRef](#)]
40. Qu, T.; Kim, Y.Y.; Yaremchuk, M. Can luzon strait transport play a role in conveying the impact of ENSO to the South China Sea? *J. Clim.* **2004**, *17*, 3644–3657. [[CrossRef](#)]
41. Zhang, Z.; Wang, W.; Qiu, B. Oceanic mass transport by mesoscale eddies. *Science*. **2014**, *345*, 322–324. [[CrossRef](#)]